Anal. Bioanal. Electrochem., Vol. 14, No. 1, 2022, 1-17

Analytical & Bioanalytical Electrochemistry

Full Paper

Crystal Structure, Morphology, Optical and Super-Capacitor Properties of Srx: α-Sb_2O_4 Nanostructures

Vinayak Adimule,[1,*] Basappa C. Yallur,[2] and Adarsha H. J. Gowda[3]

[1]*Department of Chemistry, Angadi Institute of Technology and Management (AITM), Savagaon Road, Belagavi-5800321, Karnataka, India*

[2]*Department of Chemistry, M S Ramaiah Institute of Technology, Bangalore-560054, Karnataka, India*

[3]*Centre for Research in Medical Devices, National University of Ireland, Gaillimh, Galway-H91TK33, Ireland*

*Corresponding Author, Tel.: +91(0831)2438123; Fax: +91(0831)2438123

E-Mails: adimulevinayak@yahoo.in; researcher@vinayakadimule.in

Received: 16 February 2021 / Received in revised form: 21 January 2022 / Accepted: 23 January 2022 / Published online: 31 January 2022

Abstract- Mixed orthorhombic Sr_x doped α-Sb_2O_4 (x=2,4,8 and 10 wt. %) nanostructures (NS) were successfully synthesized by simple chemical precipitation method. Crystal structure, morphologies and microstructures of the as-synthesized Sr_x: α-Sb_2O_4 NS were characterized by X-ray diffraction (XRD) and scanning electron microscopy (SEM) techniques. XRD displayed that the NS were extensively crystalized and crystallite size increases with increase in the concentration of Sr^{2+} ions. SEM revealed spherical like morphologies and grain size varies between ~ 88 nm to 110 nm. Red shift in the optical absorptivity and increase in the optical band gap (E_g) displayed in UV-visible spectra as the Sr concentration increases in α-Sb_2O_4 NS. In Fourier transform infrared spectra (FT-IR), intensity of the characteristic peak Sb-OH gradually increases as Sr^{2+} dopant concentration increases in NS. Electrochemical performances of Sr_x: α-Sb_2O_4 (x =10 wt. %) NS exhibited specific capacitance of 890 F/g at a current density of 1 A/g in 6 M KOH solution. Sr_x: α-Sb_2O_4 NS showed cyclic retention of 88.95 %, long term cyclic stability up to 1000 cycles and excellent repeatability and reproducibility. Sr_x:α-Sb_2O_4 NS act as a promising electrode material for super capacitor and can be used in high energy storage device applications.

Keywords- Cyclic voltammetry; Galvanostatic Charge-Discharge; Sr: α-Sb_2O_4; Nanostructures; UV-visible; XPS

1. INTRODUCTION

Nanostructured materials in recent years offers large surface to volume ratio (S/V) than that of corresponding bulk materials. α-Sb_2O_4 widely used for catalysis, mixed oxide catalysis as a key promoter in adsorbing oxygen during catalytic reactions. Electrochemical properties of bimetallic oxides largely dependent on the electrode materials and improvising performance of the electrode material [1] is an effective strategy to overcome the energy demand. In recent years Antimony (Sb) based electrodes attracted much attention owing their intrinsic negative over potentials, large surface to volume ration (S/V), high stability [2,3]. The issue triggered our interest in developing Sb based electrode materials by doping appropriate amount of strontium (Sr). Among various reported Sb based anodes, Sb_2O_4 possesses high theoretical capacity of 1227mAh/g as compared with other Sb based NS [4]. However, very few studies have been reported for doped Sb_2O_4 NS. According to recent investigation reports Sb2O4 reacts with Na ion, accommodates in its structure followed by alloying type of reactions. Sb_2O_4/Na possesses discharge capacities of 1120 m Ah/g, 894 m Ah/g, 764 m Ah/g for successive first, second and twenty cycles [5]. Irrespective of theoretical capacities of Sb anodes they are limited in practical use because of low reversibility, high redox potential and Sb_2O_4 suffers from large hysteresis loss [6]. Remarkable large specific capacity of the Sb based oxides (Sb_xO_y) is due to unique structural morphology and formation of alloying type of reaction during electrochemical interaction [7,8]. Antimony exists in different phases viz, Sb_2O_3, Sb_2O_4, Sb_2O_5, Sb_6O_{13} [9,10], among them Sb_2O_4 exits in two different structural configurations. α-Sb_2O_4 exists in orthorhombic configuration and β-Sb_2O_4 in monoclinic structure [10]. Inter conversion of alpha to beta phase can be done with application of temperature. In most of the cases Sb_2O_4 obtained from Sb_2O_3 and used in catalytic oxidation of methane [11]. Fu et al [8] reported reversible specific capacity of 896 m Ah/g for thin film of Sb_2O_4 NS and studied effective alloying reaction with Na. Similar to Li storage in Sb_2O_3 [12,13], Na storage in Sb_2O_4 NS [8], Sb_2O_4 naturally used as potential anode material and has large specific capacity. Theoretical specific capacity of Sb_2O_4 was 1220 m Ah/g which is 3.8 times higher than graphite. Recently Mohammed M. R, Jahir A [14] demonstrated synthesis of Cd doped Sb_2O_4 NS coated over modified carbon electrode and studied for sensitivity towards melanin. They also found higher sensitivity of 3.15 μAμ/M/cm^2 for wide range of concentrations. Sb_2O_4 composite with reduced graphene oxide (rGO) [15] synthesized by facile solvothermal approach and used as anode material for lithium-ion batteries. Composites also showed reversible specific capacity of 1170 mAh/g, cyclic stability of 798 mAh/g after 200 cycles. Recent investigation on the device architecture of different nanomaterials such as yttrium, gadolinium, zirconium and their composites employed for effective enhancement of optical, photoluminescence, electrical and electronic properties [16-22].

From the above literature evidences, in the present work author synthesized different concentrations of Sr doped Sb_2O_4 NS by co precipitation method, the samples were

characterized by SEM, SEM-EDX, XPS, XRD, UV-visible and FT-IR spectroscopic methods. The 2, 4 and 8 wt.% Sr doped Sb_2O_4 NS does not show higher specific capacitance in 6 M KOH solution. Electrochemical specific capacitance of 890 F/g at the current density of 1 A/g obtained for 10 wt.% of Sr: Sb_2O_4 NS. The cyclic stability of 88.9 % after 1000 cycles showed good electrochemical performance and Srx:Sb_2O_4 NS can be used as electrode material for super capacitor applications.

2. EXPERIMENTAL SECTION

2.1. Materials and methods

All the chemicals used in our experiments were analytical grade and procured from Sigma Aldrich, Alfa Assar Ltd. Purity of the chemicals and reagents used in the synthesis are, antimony trichloride ($SbCl_3$), (99.8%), strontium chloride hexahydrate ($SrCl_2.6H_2O$), (99.65%), cetyl trimethyl ammonium bromide (CTAB), (95.8%), thiophenol (96.8%) used without additional purification. The crystal structure, morphology and phase of as-synthesised NS were investigated using XRD patterns obtained on Rigaku mini plex with CuKα radiation. SEM images and EDX (energy dispersive-ray) were recorded using Philips XL 30 with 10x-100000x magnification. Chemical composition and valence state of the as-synthesized NS investigated using Shimadzu AXIS Supra plus instrument having parallel XPS (X-ray photoelectron spectroscopy) imaging technique. Specord 210 plus analytic jean with variable spectral resolution used for recording optical characteristics of the NS. Shimadzu Varian 4300 spectrophotometer was used to examine stretching and bending vibrations of the elements present in the NS. Electrochemical performances of the NS were carried out by using Metrohum instrument equipped with auto lab operating between 10 µHz to 32 MHz using NOVA Software for Bode, GCD, electrochemical impedance spectroscopy (EIS), and cyclic voltammetry (CV) analysis.

2.2. Synthesis of α-Sb_2O_4 NS (Step 1)

In a typical synthesis, α-Sb_2O_4 was added with $SbCl_3$ (0.25 M, 20 mL), urea (0.1 M, 10 mL) and are mixed in 20 mL of distilled water, stirred for ~2-3 h, dropwise NH_4OH was added, white precipitate agitated at 80°C for ~3 h, the reaction mixture (RM) brought to room temperature, the precipitate was filtered, washed with cold water (20 ml×2 times), absolute ethanol (10 ml×2 times) and dried at 100 °C, calcinated at 600 °C and obtained as α-Sb_2O_4 NS [23-25] (Reaction 1):

$$Sb_2Cl_3 + 4H_2O \longrightarrow Sb_2O_4 + 2H_2\,(g) + 3HCl\,(g) \qquad (1)$$

2.3. Sr Doping to α-Sb_2O_4 NS (Step 2)

Synthesis of Sr: α-Sb_2O_4 NS started with precursor Sr $Cl_3.6H_2O$ (0.15 M, 2.38 g) with equivalent wt. the ratio of Sr_x (x=2,4,8 and 10 wt. %), dissolved in distilled water, added with

20 mL of urea aqueous solution, heated at 80°C for ~4h, α-Sb_2O_4 was added and heating continued for further 3 h, RM was cooled to room temperature, added NH_4OH solution till pH of the solution becomes ~12, off white colored precipitate, was filtered, washed with water (10 ml×2 times), ethanol (5 ml×3 times), dried at 100 °C, calcinated at 600 °C and yielded as Sr_x:α-Sb_2O_4 NS, Fig. 1, (Reaction 2):

$$SrCl_3 + \alpha\text{-}Sb_2O_4 + H_2O + H^+ \longrightarrow Sr_x\text{: }\alpha\text{-}Sb_2O_4 + HCl + Cl_2\,(g) + OH^- \quad (2)$$

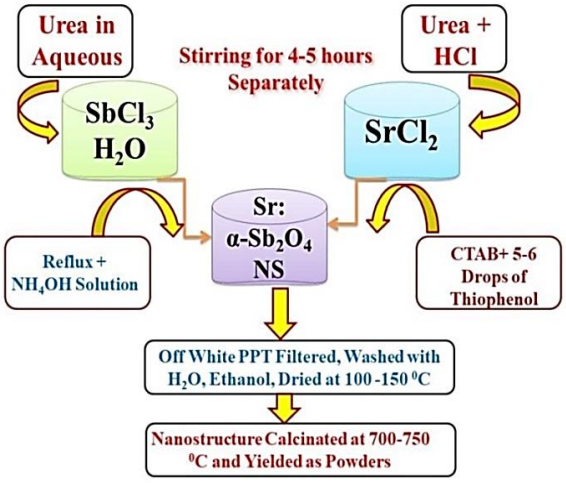

Figure 1. Schematic synthesis flow chart of Sr_x: α-Sb_2O_4 NS

2.4. Elemental Compositional Analysis of Sr: α-Sb_2O_4 NS

Nanoparticles (NPs) purity and their chemical compositions are to be investigated to understand the experimental setup needed and their analysis carried out to investigate their chemical constituents of metal or non-metal. Sr_x:α-Sb_2O_4 NPs obtained by co-precipitation method and reduced NPs interact with the solvent molecules to form MOS. Sr_x: α-Sb_2O_4 NPs populated in the crystal structure and their composition can be understood with the elemental compositional analysis. Table 1S summarizes %composition of Sr:α-Sb_2O_4 NS.

3. RESULTS AND DISCUSSION

3.1. XRD Studies

X-ray diffraction (XRD) patterns displayed (Fig. 2) crystallite phase of the peak corresponds to mixed orthorhombic for 10 wt. % of Sr: α-Sb_2O_4 NS. Only diffraction peaks of (211), (222), (411) and (431) occur in the spectra at 2θ = 26.8°, 29.7°, 34.2°, 44.3° respectively. The minimal impurity peaks suggest a strong growth texture of the Sr: α-Sb_2O_4 NS. XRD carried out with monochromatic CuKά radiation (40 kV, 50 Hz), scanned in the step of 0.03° with an angular range of 20-90° 2θ. Sr: Sb_2O_4 NS XRD pattern is almost the same as that of pure α-Sb_2O_4 NS and no additional diffraction planes are present for both the phases. The

average particle size (D) was calculated using the Debye Scherrer's equation [26] (Equation 1). The values of 2θ, FWHM, lattice parameters are summarized in Table 1.

$$D = K\lambda/\beta \cos\theta \qquad (1)$$

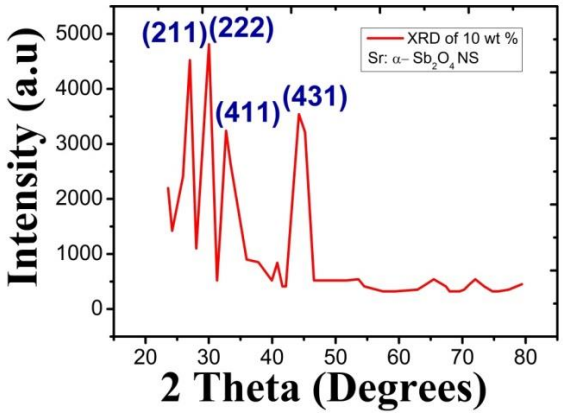

Figure 2. XRD diffraction patterns of Sr_x: α-Sb_2O_4 NS

where, λ-wavelength of X-ray radiation (0.1540 nm), K-Scherr's constant, θ-characteristics of X-ray radiation, β-FWHM (full width half maximum). An increase in the mole fraction of Sr content, size of the NPs decreases, this is due to segregation of Sr over grain boundary of α-Sb_2O_4 NS which will hinder the growth of NPs.

Table 1. XRD values of $d_{(hkl)}$, FWHM, lattice parameters, and angle shift of 10 wt.% Sr:α-Sb_2O_4 NS

Sample	2θ	$d_{(hkl)}$ (A°)	FWHM°	Lattice Parameters	Angle shift Δ 2θ (°)
(2 wt. %) Sr: α-Sb_2O_4 NS	39.15	3.812 (222)	0.2514	a= 0.2124, b=0.2478, c=0.2654	0.31
(4 wt. %) Sr: α-Sb_2O_4 NS	39.05	3.836 (222)	0.2578	a= 0.2418, b=0.2029, c=0.2578	0.34
(8 wt. %) Sr: α-Sb_2O_4 NS	39.03	3.914 (222)	0.2584	a= 0.2702, b=0.2857, c=0.2649	0.41
(10 wt. %) Sr: α-Sb_2O_4NS	38.94	3.901 (222)	0.2417	a= 0.2711, b=0.2824, c=0.2611	0.42

The average particle size of the 2 wt.%, 4 wt.%, 8 wt.%, and 10 wt.% is 36.12 nm, 37.02 nm, 38.54 nm, and 43.54 nm respectively. The diffraction patterns of the as-synthesized samples match with the JCPDS file number 11-0694. The orthorhombic phase of α-Sb_2O_4 consists of two phases, one is SbO_4 tetragonal polyhedral and another is SbO_6 octahedral which represents the overall layered structure [27] in which Sb (+5) and Sb (+6) are surrounded by

four and six O atoms. The crystallite size, morphology index, relative percentage error, texture coefficients are summarized in Table 2S.

3.2. Optical Studies

UV-visible spectroscopic technique was used to examine the optical properties of Sr:Sb_2O_4 NS. The wavelength (λ_{max}) and shoulder peak ($\lambda_{shoulder}$) for different concentrations of Sr:α-Sb_2O_4 NS were depicted in Fig. 3. Fig. 3(a) displayed a well-defined absorption spectrum for 2 wt. % of Sr: α-Sb_2O_4 NS with λ_{max}-329 nm, $\lambda_{shoulder}$ appeared at 350 nm which are characteristics of the orthorhombic type of α-Sb_2O_4 NS.

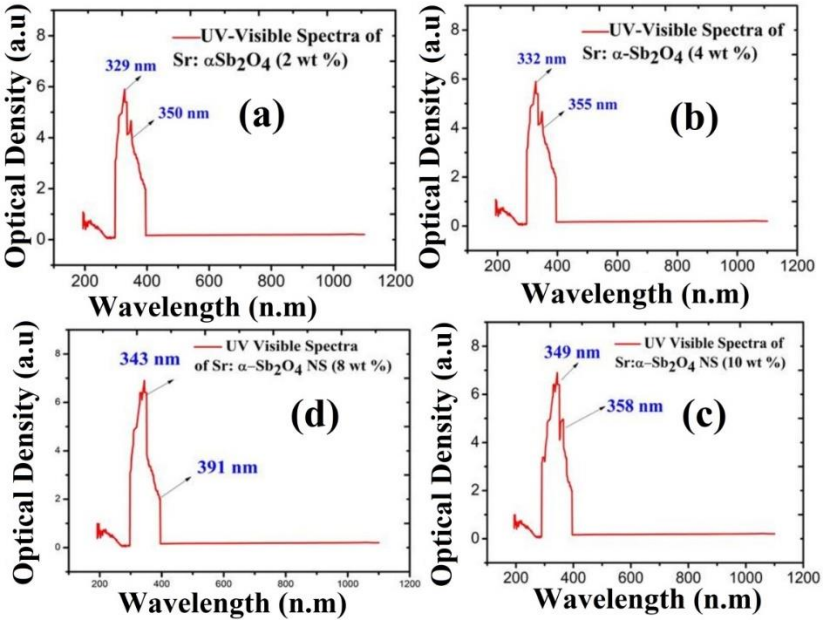

Figure 3. UV-visible spectrum of (a) Sr: α-Sb_2O_4 NS (2wt.%); (b) Sr: α-Sb_2O_4 NS (4 wt. %); (c) Sr: α-Sb_2O_4 NS (10 wt.%) and (d) Sr: α-Sb_2O_4 (8 wt.%)

Fig. 3(b), for 4 wt. % of Sr: α-Sb_2O_4 NS λ_{max} appeared at 332 nm and $\lambda_{shoulder}$ formed at 355 nm. No other impurity peak appeared which indicates fewer defects and more crystallinity of the Sr: α-Sb_2O_4 NS. 10 wt. % of Sr: α-Sb_2O_4 NS λ_{max} appeared at 349 nm and $\lambda_{shoulder}$ at 358 nm (Fig. 3(c)). For 8 wt. of Sr: α-Sb_2O_4 NS, λ_{max} appeared at 343 nm and λ_{min} at 391 nm (Fig. 3(d)) Redshift in the absorptivity or increase in absorbance towards visible or near-infrared regions is due to intraband absorption between conduction band and valance band electrons as reported in the dude absorption [28]. The reduced size of the NPs can cause the change in the optical band gap by narrowing down the spaces in between crystal structures. In order to determine optical bandgap, a graph of $(\alpha h\gamma)^2$ versus $(h\gamma)$ plotted (extrapolating the straight line $(\alpha h\gamma) = 0$) as shown in Fig. 4. The obtained values of the optical bandgap is in good agreement with those reported for Sb_2O_4 in literature [29]. Bandgap energies are

calculated by tangents drawn to intercept plots of $(\acute{a}h\gamma)^2$ Vs photon energy ($h\gamma$) as shown in Fig. 4. We found that the optical band gap decreases as the Sr concentration increases in the NS. Bandgap as calculated from the Tauc plots, for 2 wt. % Sr:α-Sb_2O_4 it is 3.1 eV, 4wt.% Sr: α-Sb_2O_4 3.22 eV, 8wt.% 3.33 eV and 10wt.% it is 3.41 eV respectively as presented in Fig. 4a, 4b, 4c, and 4d calculated using the formula as presented in Equation 2:

$$h\gamma = A\,(h\gamma - Eg)^2 \qquad (2)$$

where A absorptivity constant, γ frequency of the source radiation, and E_g is the optical gap of NS. The investigated optical absorptivity values are summarized in Table 3S.

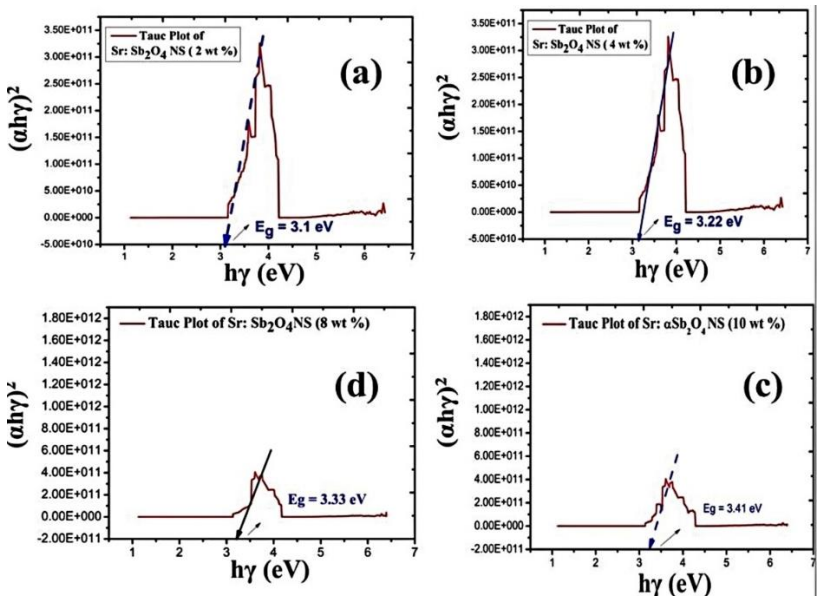

Figure 4. Tauc plot of (a) Sr: α-Sb_2O_4 NS (2 wt.%); (b) Sr: α-Sb_2O_4 NS (4 wt.%); (c) Sr: α-Sb_2O_4 NS (10 wt.%) and Sr: α-Sb_2O_4 NS (8 wt.%)

3.3 FT-IR (Fourier Transform Infra-red spectroscopy) Studies

FT-IR spectrum of an as-synthesized sample of Sr_x: α-Sb_2O_4 NS mixed with KBr powder as displayed in Fig. 5. The absorption band was recorded for 2wt.% of Sr: α-Sb_2O_4 NS appeared at ~1411 cm^{-1}, ~1650 cm^{-1}, ~3121 cm^{-1} corresponds to stretching frequencies of C=O absorbed from the environment, oxide bridge of Sr-O-Sr and Sb-OH [30] (Fig. 5a). The stretching band appeared at ~3350 cm^{-1} corresponding to the absorbed H_2O or surface hydroxyl group. For 4 wt. % of Sr:α-Sb_2O_4 NS, a shift in the wavelength towards lower frequencies with observed bands at ~1378 cm^{-1}, ~1610 $cm^{-1,}$ and ~ 2927 cm^{-1} for C=O, Sr-O-Sr and Sb-OH respectively (Fig. 5b). Bands under ~ 450 cm^{-1} to ~ 350 cm^{-1} correspond to vibrations caused by the deformation of the Sb-O-Sb bond [31]. For 10 wt. % of Sr:α-Sb_2O_4 NS the CO_2 peak appeared at ~1371 cm^{-1}, Sr-O-Sr observed at ~ 1672 $cm^{-1,}$ and Sb-OH ~ 2912 cm^{-1}. Adsorbed H_2O water molecule peak shift from ~ 3350 cm^{-1} to 3320 cm^{-1} (Fig. 5c). Band assignments and their

respective wavenumber of pure $SrCl_2$, α-Sb_2O_4, and different wt. % of Sr: α-Sb_2O_4 NS summarized in Table 4S.

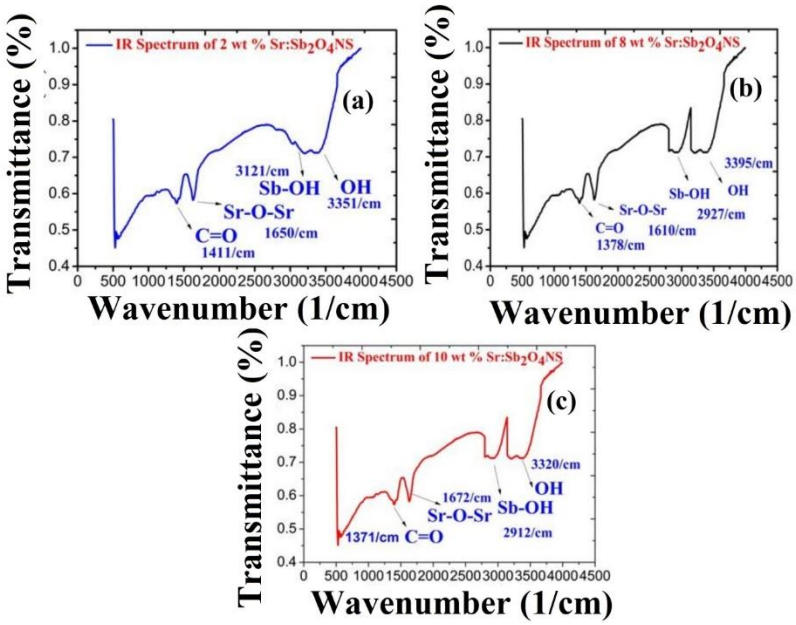

Figure 5. FTIR spectrum of 2 wt. % of Sr_x: α-Sb_2O_4 NS; (b) 8 wt. % Sr_x: α-Sb_2O_4 NS; (c) 10 wt. % of Sr_x: α-Sb_2O_4 NS

3.4. Morphology Studies

The morphology of Sr:α-Sb_2O_4 NS is displayed in Fig. 6. The top-view of the SEM revealed agglomerated NPs. It is well known from the previous literature reports surfactants play a vital role in the synthesis, the morphology of the NS [32,33].

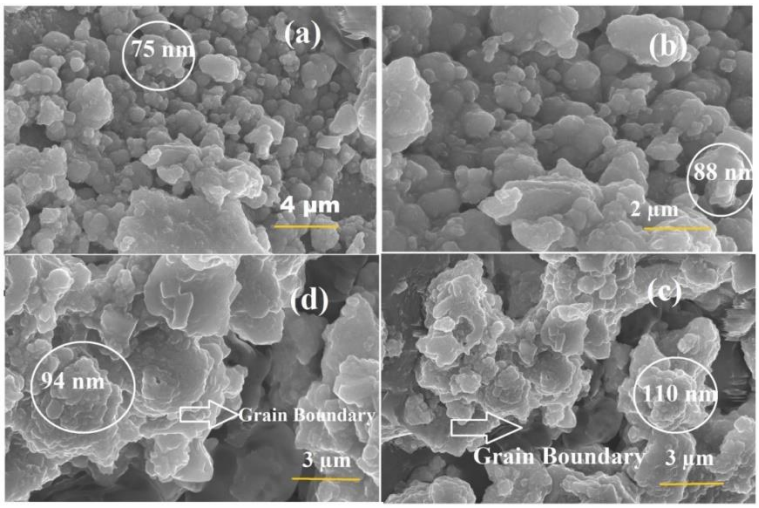

Figure 6. SEM images of (a) 2 wt.% Sr: α-Sb_2O_4 NS; (b) 4 wt.% Sr: α-Sb_2O_4 NS; (c) 8 wt.% Sr: α-Sb_2O_4 NS and (d) 10 wt.% Sr: α-Sb_2O_4 NS respectively

Fig. 6 displays morphology of 2 wt. % of Sr: α-Sb_2O_4 NS. The Sr: α-Sb_2O_4 NS exhibited flake-like morphology, which is very consistent with the reported literature [34]. Fig. 6(b), Fig. 6(c), and Fig. 6(d) displayed morphologies of 4 wt.%, 8 wt.%, and 10 wt.% of Sr: α-Sb_2O_4 NS respectively: display the SEM images show that increase in the wt. fraction of Sr^{+2} ions size of the crystal is changing and tend to become more agglomerated. Similar results have been previously reported for other nanomaterials [35-36].

SEM-EDX (energy-dispersive X-ray) spectrum of the Sr_x: α-Sb_2O_4 NS (x=2 wt.%, 4 wt.%, 8 wt.%, and 10 wt.%) as displayed in Fig. 1S with their atomic % and Net intl depicted in inset Table. The presence of Sr, Sb, and O was confirmed by EDX analysis. Atomic wt. of Sr in the selected area 1, 2, and 3 are found to be 11.31%, 18.31%, and 21.31% respectively. Whereas Sb presents in the ratio of 84.24%, 74.24%, and 70.24% respectively. All the elements and their oxygen concentration in the synthesized NS are verified and found to be in good agreement with each other (in the ratio of 10:1).

3.5. XPS Studies

In order to examine the chemical composition, valence states of various elements present in the NS, X-ray photoelectron spectroscopy (XPS) was conducted and obtained raw data and Gaussian fit data represented in Fig. 7. C1s peak (Fig. 7a) appeared at binding energies of 283.5 eV. α-Sb_2O_4 has mixed-valence states [37,38]. The Sb peak is deconvoluted into two peaks Sb $3d_{3/2}$ and Sb $3d_{5/2}$ which are assigned with binding energies of 529.8 eV and 524.5 eV with an energy separation of 5.3 eV [39]. O1s XPS spectrum (Fig .7b) appeared at 528.2 eV which is overlapped with the Sb $3d_{3/2}$ orbital with a binding energy of 529.8 eV.

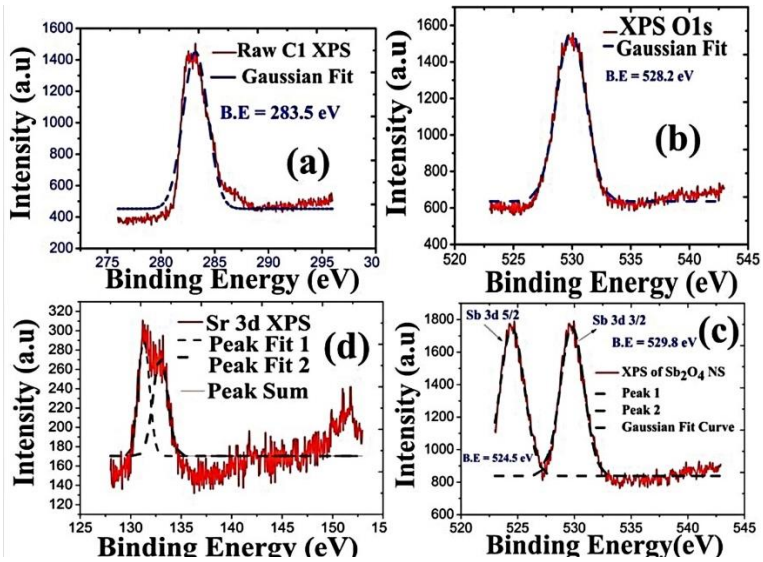

Figure 7. (a)C1s XPS spectrum (b) O1s XPS spectrum (c)XPS spectrum of Sb $3d_{3/2}$ and Sb $3d_{5/2}$ (d) XPS spectrum of Sr $3d_{3/2}$ and Sr $3d_{5/2}$ respectively

Table 2. Summarizes the binding energy, separation doublet of various metals in Sr_x:α-Sb_2O_4 NS

Peak Assignment	Binding Energy (eV)	Separation of doublet (eV)
C1s	283.5	-
Sr 3d $_{3/2}$	131.3	-
Sr 3d $_{5/2}$	133.5	2.2
Sb 3d $_{3/2}$	529.8	-
Sb 3d $_{5/2}$	524.5	5.3
O1s	528.2	-

3.6. Electrochemical measurements

3.6.1. Cyclic voltammetric experiments

Cyclic voltammetry experiments were carried out in 6 M KOH as electrolyte at different scan rates (voltage window 0 V to -1 V) and the results are as shown in Fig. 8. Compared with other electrodes, the CV curve of Sr (10 wt. %) doped NS is almost rectangular at various scan rates exhibiting ideal capacitive, good reversibility, and cyclic stability. Furthermore, when the scan rate is 50 mV/s, the CV curve is almost rectangular shape while the curves for the other electrodes deviate from the rectangular shape [40]. The performance of the electronic conduction and proton transfer happens quickly in the case of Sr (10 wt. %) doped α-Sb_2O_4 NS thereby increase in the cyclic stability and specific capacitance. The electrodes can undergo pseudo-capacitance reaction quickly at a high scan rate revealing high charge and discharge properties [41]. Capacitance is the ability to store electrical charge and can be calculated from Equation (3):

$$\Delta Q = C \times \Delta U \qquad (3)$$

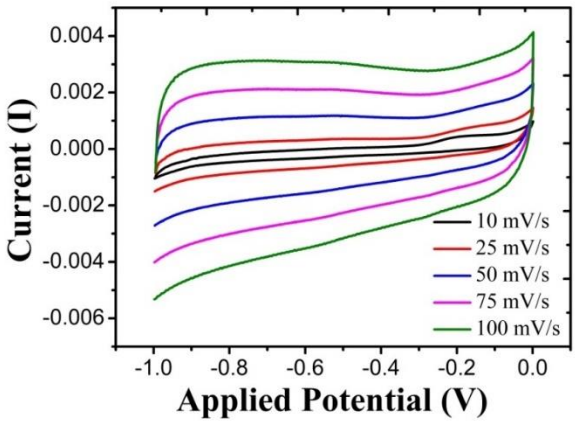

Figure 8. The cyclic voltammetric curve of Sr doped α-Sb_2O_4 NS at various scan rates

3.6.2. Galvanostatic charge-discharge cycles (GCD) experimentation

Fig. 9a shows the GCD cycles of Sr_x: α-Sb_2O_4 NS in 6 M KOH electrolyte at current densities of 0.25 A/g to 2 A/g. The discharge time of 10 wt. % Sr:α-Sb_2O_4 was found to be 138 s, 175 s, and 188 s at 0.25 A/g, 0.5 A/g and 1 A/g current densities respectively. The variation in the phase angle Vs time and real, the imaginary part of the impedance presented in Fig. 9 (b) and Fig. 9(c). Moreover compared with pure $SrCl_2$/SrO and pure α-Sb_2O_4 NS, GCD curve for Sr_x:α-Sb_2O_4 exhibits voltage drops which results in large internal resistance which demonstrates electrical conductivity of the Sr:α-Sb_2O_4 NS [42]. As the charge/discharge time extends it can be seen that charge/ discharge performs good symmetry and linear changes [43]. The capacitive retention Vs charge-discharge cycles of as-synthesized NS is shown in Fig. 9(d). The values of specific capacitance and charge/discharge efficiency can be calculated in a three-electrode system based on multiple GCD curves and Rs, Rp, CPE of the 10 wt. % Sr: α-Sb_2O_4 NS presented in Table 5S. The energy density (E) and power density (P) can be calculated using the following equations (4) and (5):

$$E = \frac{1}{2}(CV)^2 \qquad (4)$$

$$P = \frac{E}{t} \qquad (5)$$

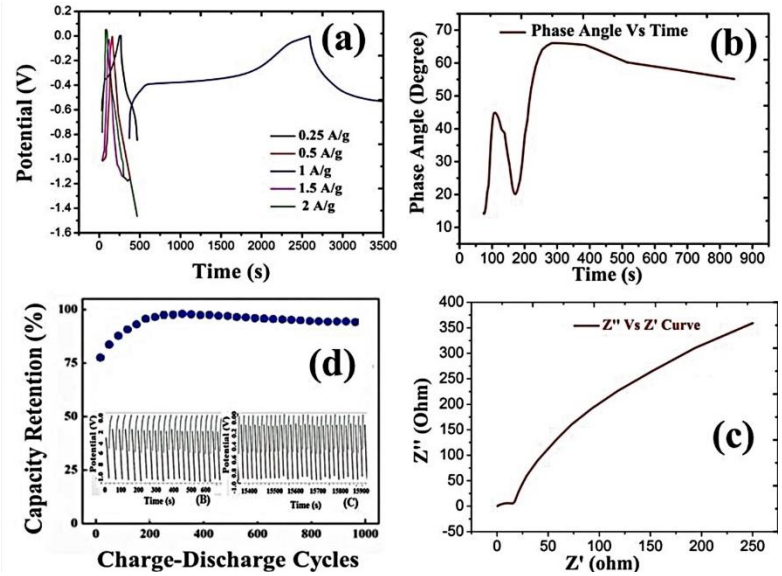

Figure 9. (a) Galvanostatic charge-discharge cycles of Sr:α-Sb_2O_4 NS (10 wt. %); (b) the relation between phase angle and time; (c) variation in the electrode resistivity (d) Capacity retention Vs charge-discharge cycles (inset showing potential Vs time)

The specific capacitance value of Sr_x: α-Sb_2O_4 NS (Fig. 10) initially was found to be 114 F/g, as the cycle number increases gradual decrease in the specific capacitance was observed slowly after 20 cycles. When the GCD reaches 1000 cycles the value of the specific capacitance was found to be 890 F/g. With the increase in the current density, the value of the specific capacitance at 1A/g was 890 F/g. The highest observed specific capacitance at 1 A/g is due to the polarization effect which enhances electrochemical reactions over the surface of the NS. Based on the initial and final specific capacitance values the capacity retention of Sr_x:α-Sb_2O_4 NS was found to be after 1000 cycles [44]. Thus, compared with other electrode systems Sr: α-Sb_2O_4 NS shows the largest specific capacitance value of 890 F/g at a current density of 1 A/g proving excellent capacitive property and stability [45].

3.6.3. EIS analysis of the Sr doped α-Sb_2O_4 NS

In general impedance, spectra are illustrated in three types small and semi arc in the high-frequency range and straight-line formation in the low-frequency range of the materials [46]. The formation of the straight line indicates the electrode process is diffusion controlled. The slope of the straight line indicates the good capacitance of the electrode [47]. The Nyquist plots are given in Fig. 10 Nyquist plots contains slopes having larger area suggesting Sr:α-Sb_2O_4 NS has good capacitance properties and the diameter of the arc has a smaller area which shows low charge/discharge resistance. Charge transfer resistance decreases upon an increase in the Sr doping. The values of Rs, Cs, and W can be obtained from the software and tabulated in Table 5S. It can be clearly seen from the values of the Rs, Cs, and W significantly smaller as compared with the pure $SrCl_2$/SrO NS indicating a decrease in the diffusion resistance for the Sr doped α-Sb_2O_4 NS which is confirmed from the Nyquist plots [48]. In CV curves the amount of charge stored depends on the current response (i) and sweep rate (υ) which is given by the equation (6):

$$i=C\upsilon^{\frac{1}{2}} \qquad (6)$$

3.6.4. Relation between Phase angle (θ) and Applied Potential

In order to understand the relation between phase angles (θ), applied potential of 10 wt. % Sr: *α*-Sb_2O_4 NS, electrochemical impedance spectroscopy (EIS) was carried out (Fig. 10). The variation of time Vs real and imaginary part of the impedance as presented in Fig. 10(a) and equivalent circuit model (ECM) obtained by cole-cole simulation of the EIS results given in Fig. 10(b). Nyquist plots obtained by plotting real part of impedance Vs imaginary part of the impedance with respect to the variation in the frequency as shown in Fig. 10(c) and Fig. 10(d) respectively. Nyquist plot contains smaller semicircle and for all the synthesized samples plots are parallel with the variation in the resistance. Dominant electrochemical reactions confirmed from the charge transfer from dopant (Sr^{+2}) ions and O^{2-} ions on the surface of *α*-Sb_2O_4 NS [49]. The decrease in the phase angle after 250 seconds confirmed effective

charge transfer between Sr^{+2} ions α-Sb_2O_4 NS. During initial stage as electrochemical reactions increases phase angle also increases which indicates effective reaction between O^{2-} and α-Sb_2O_4 NS. Experimentally obtained resistance values are found to be 1.578 Ω for SrO NPs, 1.014 Ω for α-Sb_2O_4 NPs and 10 wt. % of Sr: α-Sb_2O_4 NPs has 0.978 Ω respectively. Low charge transfer and electrical resistance of the NS enable the formation of large capacitance and good rate of discharge and recharge cycles. Table 3 summarizes specific capacitance, preparation methods, scan rate of various NS reported in the literature.

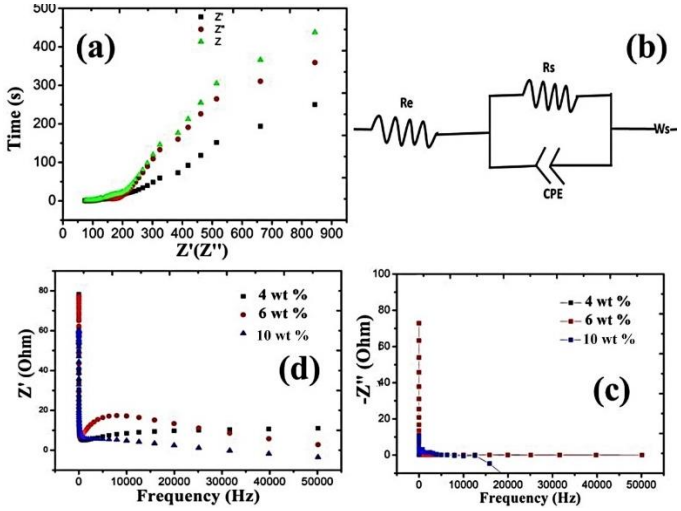

Figure 10. (a) Variation of resistance Vs time; (b) Equivalent Circuit Model (ECM) of Sr: α-Sb_2O_4 NS (c) and (d) Nyquist plot of Sr: α-Sb_2O_4 NS

Table 3. Comparison of the specific capacitance, their preparation method, and a scan rate of the different electrodes reported in the literature

Electrode Material	Preparation method	Scan Rate	Specific Capacitance (F/g)	Ref.
$NiCo_2O_4$-NiO	Galvanostatic (CV)	1	82.1	[50]
Mn-Cu binary oxides	Galvanostatic (CV)	5/0.5	422/417	[51]
Na-doped SCO	Galvanostatic (CV)	5/0.9	519.80/319	[52]
Ni_3S_2	Ni Foam	2000	1529	[53]
CC-NC-LDH	Carbon Cloth	20000	1817	[54]
Sr:α-Sb_2O_4 NS	Co-precipitation	1, 000	890	This study

4. CONCLUSION

In summary, novel series of Sr:α-Sb_2O_4 NS was successfully synthesized by the simple precipitation method and characterized by XRD, SEM, UV-visible, FT-IR, and elemental analysis. Flake-like morphology and mixed-phase of orthorhombic crystal structure confirmed from SEM and XRD studies. An increase in Sr content over α-Sb_2O_4 NS causes a redshift in optical absorptivity and shift in the Sb-OH bond confirmed by UV-visible and FT-IR spectroscopic investigation. The discharge tests show that Sr_x: α-Sb_2O_4 (x=10 wt.%) has a specific capacitance of 890 F/g at a current density of 1 A/g and the value remains constant after 1000 cycles with 88.95 % retention. The results of the electrochemical tests exhibited a remarkable increase in the specific capacitance value for Sr_x: α-Sb_2O_4 NS as compared with pure $SrCl_2$/SrO and pure Sb_2O_4. Therefore Sr:Sb_2O_4 NS become a novel application in improvising energy harvesting devices as compared with pure Sb_2O_4 NS.

Acknowledgment

Authors are thankful to IIT Kanpur for SEM, SEM EDX and XPS analysis, MSRIT, Bangalore CV, XRD, UV-visible, and elemental compositional investigations. Central University of Karnataka, Kalburgi for CV, EIS analysis

Declarations

Funding

Authors do not have received any funding from any institutions or agencies.

Conflict of interests

All the authors declare that they do not have any competing interests.

Availability of data

All data generated or analyzed during this study are included in this published article. Further data can be obtained by the corresponding author on request.

Code Availability

"Not Applicable"

Authors Contributions

Dr. Vinayak Adimule contributed to synthesis, manuscript preparation, Dr. Yallur BC was involved in the characterization of the samples and Mr. Adarsha HJ Gowda was involved in the measurement of the supercapacitor properties of the nanostructures.

REFERENCES

[1] G. Wang, L. Zhang, and J. Zhang, Chem. Soc. Rev. 41 (2012) 797.
[2] M. U. A. Prathap, and R. Srivasta, J. Polym. Res. 18 (2011) 2455.
[3] O. Tovide, N. Jaheed, N. Mohamed, E. Nxusani, C. Sunday, and A. Tsegaye, Electrochim. Acta. 128 (2014) 138.
[4] H. Hou, M. Jing, Z. Huang, Y. Yang, Y. Zhang, J. Chen, Z. Wu, and X. Ji, ACS Appl. Mater. Interfaces 7 (2015) 19362.
[5] Q. Sun, Q. Q. Ren, H. Li, Z. and W. Fu, Electrochem. Commun. 13 (2011) 1462.
[6] F. Klein, B. Jache, A. Bhide, and P. Adelhelm, Phys. Chem. Chem. Phys. 15 (2013) 15876.
[7] M. Hu, Y. Jiang, W. Sun, H. Wang, C. Jin, and M. Yan, ACS Appl. Mater. Interfaces. 6 (2014) 19449.
[8] Q. Sun, Q. Q. Ren, H. Li, Z. W. Fu, Electrochem. Commun. 13 (2011) 1462-1464.
[9] S.E. Golunski, and D. Jackson, Appl. Catal. 48 (1989) 123.
[10] D. Orosel, P. Balog, H. Liu, J. Qian, and M. Jansen, J. Solid State Chem. 178 (2005) 2602.
[11] M.O. Guerrero-Perez, T. Kim, M.A. Banares, and I.E. Wachs, J. Phys. Chem. C. 114 (2008) 16858.
[12] H. Li, X. Huang, and L. Chen, Solid State Ion. 123 (1999) 189.
[13] A. Bitner-Michalska, K. Michalczewski, J. Zdunek, A. Ostrowski, G. Zukowska, T. Trzeciak, E. Zero, J. Syzdek, and M. Marcinek, Electrochim. Acta 210 (2016) 395.
[14] M. M. Rahman and J. Ahmed, Biosens. Bioelectron. 102 (2018) 631.
[15] X Zhou, Z. Zhang, X. Lu, X. Lv, G. Ma, Q. Wang, and Z. Lei, ACS Appl. Mater. Interfaces 9 (2017) 34927.
[16] A, Vinayak. B. C. Yallur, M. Challa, and R. S. Joshi, Heliyon, 7 (2021) e08541.
[17] A. Vinayak, B. C. Yallur, and K. Sharma, J. Optics (2021) 1.
[18] S. Anusha, V. Adimule, and S. S. Nandi, Macromol Symp, 392 (2020) 2000002.
[19] A. Vinayak, B. C. Yallur, D. Bhowmik, and A. H. J. Gowda, Trans. Electric. Electron. Mater. 1-16. (2021)
[20] A. Vinayak, M. G. Revaigh, and H. J. Adarsha, J. Mater. Eng. Perf. 29 (2020) 4586.
[21] A. Vinayak, R. G. Revaiah, S. S. Nandi, and A. H. Jagadeesha. Synthesis, Electroanalysis 33 (2021) 579.
[22] A. Vinayak, A. Suryavanshi, B.C. Yallur and S. S. Nandi. Macromol. Symp, 392 (2020) 2000001.
[23] A. Vinayak, D. Bhowmik, and A. H.J. Gowda, Macromol. Symp, 400 (2021) 2100065.
[24] A. Vinayak, B. C. Yallur, D. Bhowmik, and A. H. J. Gowda. J. Mater. Sci. Mater. Electron. 32 (2021) 12164.
[25] [25] A. Vinayak, D. Bhowmik, and A. Suryavanshi, Mater. Sci. Eng. 577 (2019) 012032.

[26] B. D. Cullity, Elements of X-ray diffraction, 2nd Edn. Addision Wesley, London (1978).
[27] P. Charton, and P. Armand, J. Non-Cryst. Solids 316 (2003) 189.
[28] J. I. Pankove, Optical Processes in Semiconductors; Dover Publications: New York, (1971).
[29] B. Ouni, M. H. Lakhdar, R. Boughalmi, T. Larbi, A. Boukhachem, A. Madani, K. Boubaker, M. Amlouk, J. Non. Cryst. Solids 367 (2013) 1.
[30] G. K. Semin and A. A. Boguslavsky, Chem. Phys. Lett. 251 (1996) 250.
[31] E. I. Voit, A. E. Panasenko and L. A. Zemnukhova, J. Struct. Chem. 50 (2009) 60.
[32] J. Zeng, Y. Zheng, M. Rycenga, J. Tao, Z.Y. Li, Q. Zhang, Y. Zhu, and Y. Xia, Am. Chem. Soc. 132 (2010) 8552.
[33] B. J. Wiley, Y. Chen, J. M. McLellan, Y. Xiong, Z.Y. Li, D. Ginger and Y. Xia, Nano Lett. 7 (2007) 1032.
[34] Y. Ao, J. Xu, D. Fu, X. Shen and C. Yuan, Colloids Surf. A Physicochem. Eng. Aspects, 312 (2008) 125.
[35] S. Liu, B. Wen, W. Jiang, C. Liu, W. Ding, N. Wang, W. Chai, Ceram. Int., 40 (2014) 15991.
[36] Q. Shi, J. Zhang, D. Zhang, C. Wang, B. Yang, B. Zhang, W. Wang, Mater. Sci. Eng. B 177 (2012) 689.
[37] T. Ji, M. Tang, L. Guo, X. Qi, Q. Yang, and H. Xu, Solid State Commun. 133 (2005) 765.
[38] G. Ren, C. Wang, J. Xia, J. Liu, and H. Zhong, Mater. Lett. 63 (2009) 605.
[39] J. Moulder, W. Stickie, P. Sobal, and K. Bomber, in: Handbook of X-ray Photoelectron Spectroscopy, Perkin Elmer, Eden Prairie (1992).
[40] B. Wang, J. Park, C. Wang, H. Ahn, and G. Wang, Electrochim. Acta, 55 (2010) 6812.
[41] K. Sathishkumar, N. Shanmugam, N. Kannadasan, S. Cholan, and G. Viruthagiri, Mater. Sci. Semicond Process 27 (2014) 846.
[42] H. Guillen-Bonilla, V. M. Rodríguez-Betancourtt, J. T. Guillen-Bonilla, J. Reyes-Gomez, L. Gildo-Ortiz, M. Flores-Martínez, M. L. Olvera-Amador, and J. Santoyo-Salazar, J. Nanomater, (2015) 979543.
[43] L. Yuan, X. H. Lu, X. Xiao, T. Zhai, J. Dai, F. Zhang, B. Hu, X. Wang, L. Gong, J. Chen, C. Hu, Y. Tong, J. Zhou, and Z. Lin Wang, ACS Nano 6 (2012**)** 656.
[44] G. Cai, X. Wang, M. Cui, P. Darmawan, J. Wang, A. Lee-Sie Eh, P. S. Lee, Nano Energy 12 (2015) 258.
[45] P. K. Kalambate, R. A. Dar, S. P. Karna, A. K. Srivastava, J. Power Sources 276 (2015) 262.
[46] M. N. Ashiq, M. J. Iqbal, and I. H. Gul, J. Magn. Magn., 323 (2011) 259.
[47] L. Liu, A. Das, and C. M. Megaridis, Carbon 69 (2014) 1.
[48] M. N. Ashiq, M. J. Iqbal, I. H. Gul, J. Magnetism Magnetic Mater. 323 (2011) 259.

[49] L. Ji, J. Wang, L. Guo and Z. Chen, J. Mater. Chem. A 5 (2017) 5178.
[50] J. Zhang, F. Liu, J. P. Cheng, and X. B. Zhang, ACS Appl. Mater. Interfaces 7 (2015) 17630.
[51] Z. Wang, J. Zhu, P. Sun, P. Zhang, Z. Zeng, S. Liang, and X. Zhu, J. Alloy Compd. 598 (2014) 166.
[52] H. R. Barai, J. Electrochem. Soc. 167 (2020) 126516.
[53] Z. Xing, Q. Chu, X. Ren, C. Ge, A.H. Qusti, A.M. Asiri, A.O. Al-Youbi, and X. Sun, J. Power Sources 245 (2014) 463.
[54] S. Li, C. Yu, J. Yang, C. Zhao, M. Zhang, H. Huang, Z. Liu, W. Guo, and J. Qiu, Energy Environ. Sci. 10 (2017) 1958.